Intermetallics 102 (2018) 34–45

Contents lists available at ScienceDirect

Intermetallics

journal homepage: www.elsevier.com/locate/intermet

Influence of Ni on the refinement and twinning of primary Cu_6Sn_5 in Sn-0.7Cu-0.05Ni

J.W. Xian[a,*], M.A.A. Mohd Salleh[b], S.A. Belyakov[a], T.C. Su[a], G. Zeng[a,c,**], K. Nogita[c], H. Yasuda[d], C.M. Gourlay[a]

[a] Department of Materials, Imperial College, London, SW7 2AZ, United Kingdom
[b] Centre of Excellence Geopolymer and Green Technology, School of Materials Engineering, Universiti Malaysia Perlis (UniMAP), Taman Muhibbah, 02600, Jejawi, Arau, Perlis, Malaysia
[c] Nihon Superior Centre for the Manufacture of Electronic Materials (NS CMEM), School of Mechanical and Mining Engineering, The University of Queensland, 4072, St Lucia, Queensland, Australia
[d] Department of Materials Science and Engineering, Kyoto University, Sakyo-ku, Kyoto, 606-8501, Japan

ARTICLE INFO

Keywords:
A. Intermetallics
B. Twinning
C. Crystal growth
Joining
F. Electron backscatter diffraction

ABSTRACT

The influence of Ni on the size and twinning of primary Cu_6Sn_5 crystals in Sn-0.7Cu-0.05Ni and Sn-xCu (x = 0.7, 0.9, 1.1) (mass%) solder joints is studied using synchrotron radiography and SEM-based EBSD. It is shown that the Ni addition does not cause significant refinement of primary Cu_6Sn_5 if the alloy is fully melted. However, for peak temperatures $\leq 250\,^{\circ}C$ relevant to industrial soldering, primary Cu_6Sn_5 are not completely melted in Sn-0.7Cu-0.05Ni and there are 10–100 times more numerous and smaller crystals than in Sn-0.7Cu. X-shaped Cu_6Sn_5 crystals with an angle of $\sim 70^{\circ}$ commonly formed in Sn-0.7Cu-0.05Ni/Cu joints and are shown to be penetration twins. This type of growth twinning was only found in partially melted samples, both in Sn-0.7Cu-0.05Ni/Cu joints and binary Sn-1.1Cu alloy. The frequency of twinned crystals was significantly higher in Ni-containing solders. The results are discussed in terms of the influence of Ni on the Cu_6Sn_5 liquidus slope and on the lattice parameters of $(Cu,Ni)_6Sn_5$.

1. Introduction

Pb-free solder compositions commonly contain a dilute Ni addition. For example, the composition Sn-0.7Cu-0.05Ni (mass%) has been in industrial use since 1999 [1], and Ni is increasingly added to Sn-Ag-Cu-X [2] and next-generation solder compositions [3,4]. The addition of Ni significantly affects the intermetallic reaction layers between the solder and copper [5]; a ~500 ppm Ni addition suppresses the formation of the Cu_3Sn layer [6–9] and results in a finer and smaller $(Cu,Ni)_6Sn_5$ layer after reflow [8,10]. The influence of Ni on the Cu_6Sn_5 layer has been linked to the substantial solubility of Ni in $(Cu,Ni)_6Sn_5$ [6] which can contain up to ~25 at% Ni [11–14]. Ni stabilises the simpler hexagonal polymorph of Cu_6Sn_5 [15] and improves the high shear rate performance of BGA joints [2,16,17]. Previous work has explored orientation relationships between Cu_6Sn_5 and the Cu substrate, where the Cu_6Sn_5 morphology has been shown to depend on the orientation of the underlying copper [18–22]. It has further been shown that Ni can alter the Cu_6Sn_5 layer growth texture [23].

When tin-based alloys are soldered on copper substrates, Cu dissolution increases the liquid composition such that primary Cu_6Sn_5 crystals form during solder solidification [24–28] even when Cu-free solders are used [24]. Cu_6Sn_5 rods can span the entire solder ball diameter [29,30] and large Cu_6Sn_5 rods have been shown to be deleterious to ball shear impact properties [31]. Similar to the $(Cu,Ni)_6Sn_5$ reaction layer, Ni additions significantly influence the formation of primary Cu_6Sn_5 in the bulk solder. Solders containing nickel usually have significantly smaller and more numerous primary Cu_6Sn_5 rods/particles in the bulk solder compared with Ni-free solders [14,32–38]; and various papers on Ni-containing solders contain micrographs of primary Cu_6Sn_5 crystals with an X-shaped morphology [10,39–42].

At present, the mechanism responsible for Cu_6Sn_5 size refinement is unclear [32] and no explanation was found in the literature for the X-shaped growth of Cu_6Sn_5 in Ni-containing solders. Therefore, the aims of this work were (i) to quantify the influence of Ni on the size of primary Cu_6Sn_5; (ii) to uncover the mechanism for the size refinement of Cu_6Sn_5 due to Ni additions, (iii) to understand X-shaped Cu_6Sn_5

* Corresponding author.
** Corresponding author. Department of Materials, Imperial College, London, SW7 2AZ, United Kingdom.
E-mail addresses: j.xian@imperial.ac.uk (J.W. Xian), g.zeng@imperial.ac.uk (G. Zeng).

https://doi.org/10.1016/j.intermet.2018.08.002
Received 8 June 2018; Received in revised form 2 August 2018; Accepted 4 August 2018
Available online 31 August 2018
0966-9795/

Table 1
Compositions of Sn-0.7Cu-0.05Ni, Sn-0.7Cu, Sn-0.9Cu and Sn-1.1Cu in mass%, as measured by XRF spectroscopy. Zn, Al, Cd, Ge are all < 0.001 mass%.

Alloy	Sn	Cu	Ni	Pb	Ag	Fe	Sb	Bi	As
Sn-0.7Cu-0.05Ni	Bal	0.699	0.053	0.026	< 0.001	0.001	0.002	0.013	0.004
Sn-0.7Cu	Bal	0.674	0.002	0.004	0.016	0.003	0.020	< 0.001	< 0.001
Sn-0.9Cu	Bal	0.852	0.006	0.022	< 0.001	0.007	0.006	0.003	0.001
Sn-1.1Cu	Bal	1.080	0.004	0.013	< 0.001	0.001	0.018	0.002	0.002

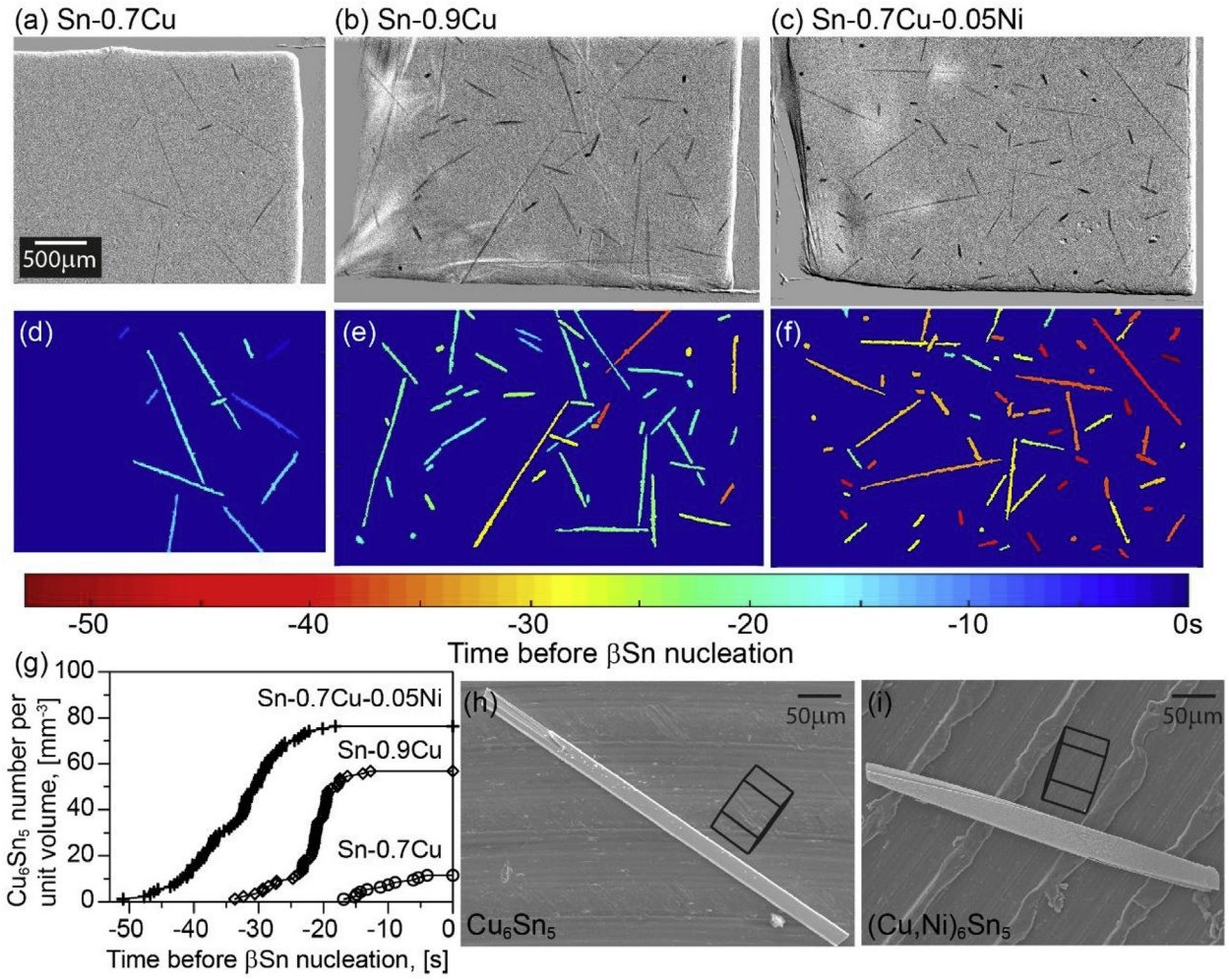

Fig. 1. (a)–(c) Synchrotron radiographs of (a) Sn-0.7Cu, (b) Sn-0.9Cu and (c) Sn-0.7Cu-0.05Ni cooled from 400 °C at ~0.33 K/s. (d)–(f) Processed maps corresponding to (a)–(c) where each Cu_6Sn_5 has been segmented and coloured by its nucleation time. t = 0s is the last frame prior to βSn nucleation. (g) Nucleation kinetics of primary Cu_6Sn_5 quantified from (d)–(f). (h–i) Typical extracted Cu_6Sn_5 crystals from Sn-0.7Cu and Sn-0.7Cu-0.05Ni respectively. Unit cell wireframes show orientations measured by EBSD.

crystal growth, and (iv) explore links between the size refinement and X-shaped Cu_6Sn_5 growth in Ni-containing solders. These aims are addressed by combining *in situ* synchrotron radiography of Cu_6Sn_5 solidification with post mortem Scanning Electron Microscopy (SEM)-based Electron Back-Scattered Diffraction (EBSD) and Energy Dispersive Spectroscopy (EDS).

2. Methods

Sn-0.7Cu, Sn-0.9Cu, Sn-1.1Cu and Sn-0.7Cu-0.05Ni solder alloys with compositions in Table 1 were used in this work. Three solder forms were studied: (i) 100 μm foils produced by rolling solder ingots; (ii) ~500 μm diameter balls produced by punching foils to discs and re-melting under flux; and (iii) commercial solder pastes.

Synchrotron radiography of soldering and solidification was conducted on beamlines BL20B2 and XU at the SPring-8 synchrotron in Hyogo, Japan, using techniques described previously [28,32,43]. For freestanding solders, 100 μm thick solder foils were held within a polytetrafluoroethylene (PTFE) cavity bounded by a quartz cell with a spacing of ~100 μm. A solder foil specimen was inserted into a furnace and heated to 400 °C at 0.33 K/s, before being cooled at ~0.33 K/s. The field of view was ~5 × 5 mm^2 recorded at 1000 × 1000 pixels at 16

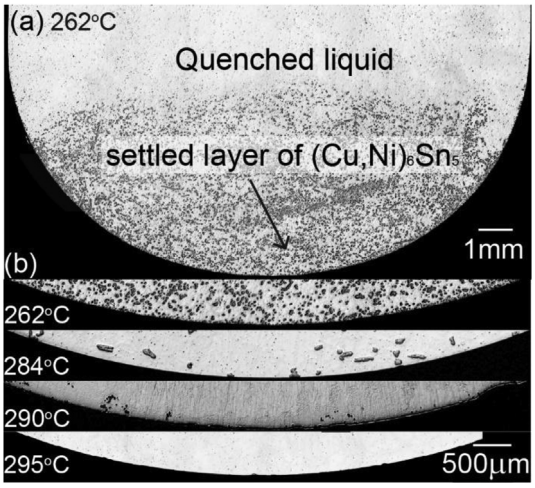

Fig. 2. (a) A settled layer of unmelted $(Cu,Ni)_6Sn_5$ crystals in Sn-0.7Cu-0.05Ni held at 262 °C for 24 h then quenched. (b) The bottom part of samples held at 262 °C, 284 °C, 290 °C and 295 °C. N.B. there is no primary $(Cu,Ni)_6Sn_5$ at 295 °C.

bit-depth, and two samples were placed side by side with each occupying half the field of view. Across the field of view the temperature difference was ~1 K. For solder joints, solder paste was used on top of ~100 μm thick Copper Organic Solderability Preservative (Cu-OSP) or Electroless Nickel Immersion Gold (ENIG) substrates. The peak temperature was 250 °C with a cooling rate of ~0.5 K/s, and the field of view was recorded at 1920 × 1440 pixels with a pixel size of 0.477 μm. In all cases, the radiographs were recorded at 1 frame per second.

To quantify the effect of peak temperature and cooling rate on the size of primary Cu_6Sn_5 in Sn-0.7Cu and Sn-0.7Cu-0.05Ni, ~500 μm diameter free standing solder balls, and solder joints made of solder balls and foils were prepared in a Mettler Toledo DSC1 and a LFR400HTX TORNADO reflow oven. Cooling rates of 0.03 and 0.33 K/s were applied in the DSC and ~3 K/s in the reflow oven. Peak temperatures of 250 °C, 300 °C and 400 °C were studied.

To reveal the 3D distribution of Cu_6Sn_5 crystals in solder joints, βSn was partially etched using a water solution of 5% NaOH and 3.5% 2-nitrophenol. An Auriga field-emission gun SEM equipped with an Oxford Instruments INCA x-sight energy dispersive x-ray (EDX) detector and a Bruker electron backscatter diffraction (EBSD) detector was used to study microstructure, compositions and crystallography. EBSD indexing was conducted using the hexagonal Cu_6Sn_5 phase [44,45] in all cases and to explore the twinning of Cu_6Sn_5 in Sn-0.7Cu-0.05Ni and Sn-1.1Cu. Note that Ni dissolves in hexagonal Cu_6Sn_5 as $(Cu,Ni)_6Sn_5$, and we refer to this simply as Cu_6Sn_5 in the rest of the paper.

Synchrotron radiographs were analysed with a combination of Matlab (Mathworks, Natick, MA, USA) and DaVis 8.3 digital image correlation (DIC) software (LaVison Imaging Company, Göettingen, Germany). For stationary Cu_6Sn_5, Matlab was used to define the solidification time of each pixel in Cu_6Sn_5 crystals as the sharp change in the intensity vs. time curve of each pixel. The nucleation time of each Cu_6Sn_5 crystal was defined as the time of the first solidified pixel in that Cu_6Sn_5 crystal. For moving Cu_6Sn_5 crystals, shift and rotation correction function in Davis was used to align radiographs accounting for both rotation and translation. The growth of the realigned Cu_6Sn_5 crystals were then tracked in Matlab. The movement of primary $(Cu,Ni)_6Sn_5$ particles due to gravity and liquid flow was analysed using DIC with correlation subset size 161 × 161 pixels^2 and correlation step of 40 pixels.

3. Results and discussion

3.1. Primary Cu_6Sn_5 formation in bulk solders

Fig. 1 compares the effects of Ni on the formation of primary Cu_6Sn_5 crystals during the solidification of Sn-0.7Cu, Sn-0.9Cu and Sn-0.7Cu-0.05Ni (mass%) bulk solders using *in situ* synchrotron imaging. The radiographs in Fig. 1(a–c) are at the end of primary Cu_6Sn_5 growth, and the coloured maps in Fig. 1(d–f) are processed images where each Cu_6Sn_5 rod has been segmented and coloured by its nucleation time. Note that t = 0s is defined as the last moment prior to βSn nucleation (in undercooled liquid) and 'hotter' colours mean that Cu_6Sn_5 nucleation occurs earlier at higher temperatures. The peak temperature was 400 °C and the cooling rate was ~0.33 K/s in all three cases. The nucleation kinetics of primary intermetallics were quantified from the radiograph sequences and are shown in Fig. 1(g). It can be seen that new Cu_6Sn_5 crystals nucleate continuously over a range of temperatures during cooling until saturating at a final number density. Note that the finest Cu_6Sn_5 crystals observed in Fig. 1 have a length of ~50 μm or a width of ~20 μm, which are well above the resolution limit of 5 μm. The final number density of primary Cu_6Sn_5 crystals in Sn-0.7Cu-0.05Ni is slightly higher than that in Sn-0.9Cu and there are approximately 5 times more crystals in Sn-0.9Cu than in Sn-0.7Cu.

In Sn-0.7Cu-0.05Ni, the Ni content in Cu_6Sn_5 rods such as in Fig. 1(c) was 7 ± 1 at% Ni (measured by SEM-EDS). The morphology of primary Cu_6Sn_5 was not significantly influenced by Ni in Fig. 1; both with and without Ni, primary Cu_6Sn_5 grew as long rods with near-random rod orientations relative to the field of view. Fig. 1(h–i) show typical SEM images of extracted Cu_6Sn_5 rods and the respective unit cells measured by EBSD. The growth crystallography remains unchanged; the Cu_6Sn_5 grows in the [0001] direction and is bounded by $\{10\bar{1}0\}$ facets with and without Ni.

It is clear in Fig. 1(g) that the first Cu_6Sn_5 nucleated significantly earlier (at higher temperature) in Sn-0.7Cu-0.05Ni than in Sn-0.9Cu, indicating that Sn-0.7Cu-0.05Ni has a higher Cu_6Sn_5 liquidus temperature. To measure the approximate Cu_6Sn_5 liquidus, ~90 g of Sn-0.7Cu-0.05Ni was held in quartz ampoules at various temperatures for 24 h and was then quenched in water. As shown in Fig. 2, a clear settled layer of Cu_6Sn_5 was present at the bottom of the sample at 262 °C, 284 °C and 290 °C, and no settled layer was present at 295 °C. From a series of such experiments, the Cu_6Sn_5 liquidus temperature of Sn-0.7Cu-0.05Ni was measured to be 292.5 ± 2.5 °C. From this it can be seen that the 500 ppm Ni addition moves the alloy into the Cu_6Sn_5 primary phase field and greatly steepens the Cu_6Sn_5 liquidus surface compared with the Cu_6Sn_5 liquidus line in binary Sn-Cu alloys. This is reasonably consistent with predictions from the Thermo-Calc TCSLD3 database [46].

Fig. 3 shows (a) the Sn-Cu phase diagram [46] and (b) the Sn rich corner of the Sn-Cu-Ni liquidus projection using data from Refs. [14,47]. The liquid compositions of Sn-0.7Cu-0.05Ni are plotted at various temperatures as an 'x' in Fig. 3(b) based on XRF measurements of quenched liquid above the settled Cu_6Sn_5 layers in experiments such as those in Fig. 2. Based on Fig. 3(a–b) and Ni contents in Cu_6Sn_5 at different equilibrium temperatures, Fig. 3(c) plots the mass fraction of

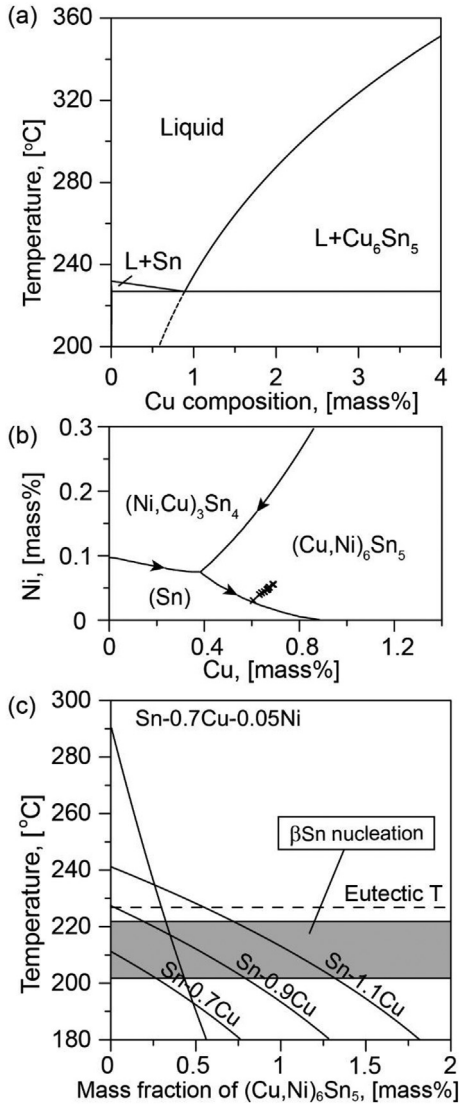

Fig. 3. (a) Sn-Cu phase diagram from Ref. [46] where dashed lines are extended liquidus lines. (b) Sn-rich corner of the Cu-Ni-Sn liquidus projection plotted using data from Refs. [14,47]. Datapoints 'x' are the measured liquid compositions. (c) Calculated mass fraction of primary Cu_6Sn_5 versus temperature.

primary Cu_6Sn_5 versus temperature, assuming that βSn does not nucleate, for the three alloys in Fig. 1 (and Sn-1.1Cu which is discussed later). It can be seen that Sn-0.7Cu-0.05Ni has a high liquidus temperature of ~292.5 °C and a much steeper temperature versus mass% primary Cu_6Sn_5 curve than Sn-0.9Cu and Sn-0.7Cu.

The nucleation undercooling of βSn was in the range ~5–25 K in synchrotron samples as indicated by the shaded area in Fig. 3(c). At 10 K undercooling, Sn-0.7Cu-0.5Ni and Sn-0.9Cu are predicted to have the same mass fraction of primary Cu_6Sn_5 of ~0.4 mass%, and Sn-0.7Cu-0.5Ni has a higher mass% Cu_6Sn_5 than Sn-0.9Cu when the βSn undercooling is smaller than 10 K. Sn-0.7Cu is predicted to contain primary Cu_6Sn_5 only when the βSn undercooling exceeds ~15 K. Multiple Sn-0.7Cu synchrotron samples were run and one solidified with no primary Cu_6Sn_5 crystals, which is likely to be due to a βSn nucleation undercooling smaller than 15 K in that experiment. Thus, the measurements in Fig. 1(g) are in reasonable agreement with the phase diagram calculations in Fig. 3(c). However, the nucleation undercoolings could not be accurately measured in the synchrotron experiment setup used in this work.

The key result in this section is that the Ni addition does not strongly affect the number density of primary Cu_6Sn_5 when bulk alloys are cooled from a peak temperature higher than the Cu_6Sn_5 liquidus temperature.

3.2. Primary Cu_6Sn_5 in joints on Cu and ENIG substrates

Fig. 4 overviews synchrotron imaging of solder joint solidification on Cu and ENIG substrates. Fig. 4a-b are radiographs of solder joints made of Sn-0.7Cu on Cu and ENIG substrates with a peak temperature of 250 °C. The radiographs are at the end of primary Cu_6Sn_5 growth (t = −1s) in undercooled liquid. It can be seen that most Cu_6Sn_5 nucleate and grow in the liquid away from the Cu_6Sn_5 reaction layer and that some Cu_6Sn_5 grow out from the layer (e.g. in the Sn-0.7Cu/ENIG sample in Fig. 4(b)). Fig. 5(a–b) are processed images of Sn-0.7Cu on Cu and ENIG, and the quantified nucleation kinetics are shown in Fig. 5(c). Each Cu_6Sn_5 rod has been segmented and coloured by its nucleation time. Note that t = 0s is defined as the first frame observed after βSn nucleation and 'hotter' colours mean that Cu_6Sn_5 nucleation occurs earlier at higher temperatures as in Fig. 1. Fig. 5(c) shows that, similar to freestanding solders in Fig. 1, Cu_6Sn_5 nucleates over a wide range of temperatures and Fig. 5(a) and (b) show that they only grow in one crystallographic direction, [0001].

Fig. 4c-d are synchrotron radiographs of solder joint solidification of Sn-0.7Cu-0.05Ni on Cu and ENIG with a peak temperature of 250 °C.

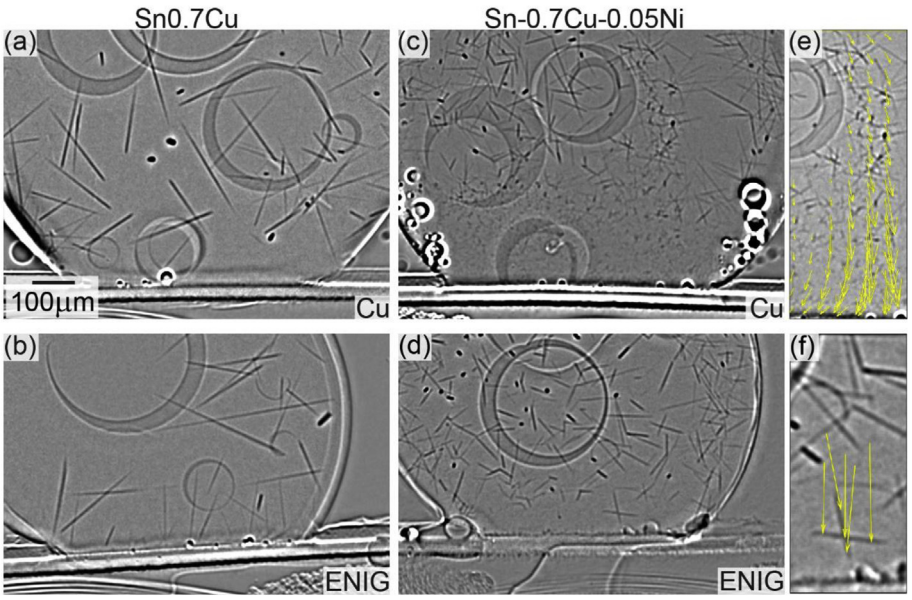

Fig. 4. Synchrotron images of (a) Sn-0.7Cu/Cu, (b) Sn-0.7Cu/ENIG, (c) Sn-0.7Cu-0.05Ni/Cu, (d) Sn-0.7Cu-0.05Ni/ENIG cooled at ~0.5 K/s from a peak temperature of 250 °C. The motion of some Cu_6Sn_5 crystals in (c,d) is tracked in (e,f) using digital image correlation, where yellow arrows are the displacement vectors. (For interpretation of the references to colour in this figure legend, the reader is referred to the Web version of this article.)

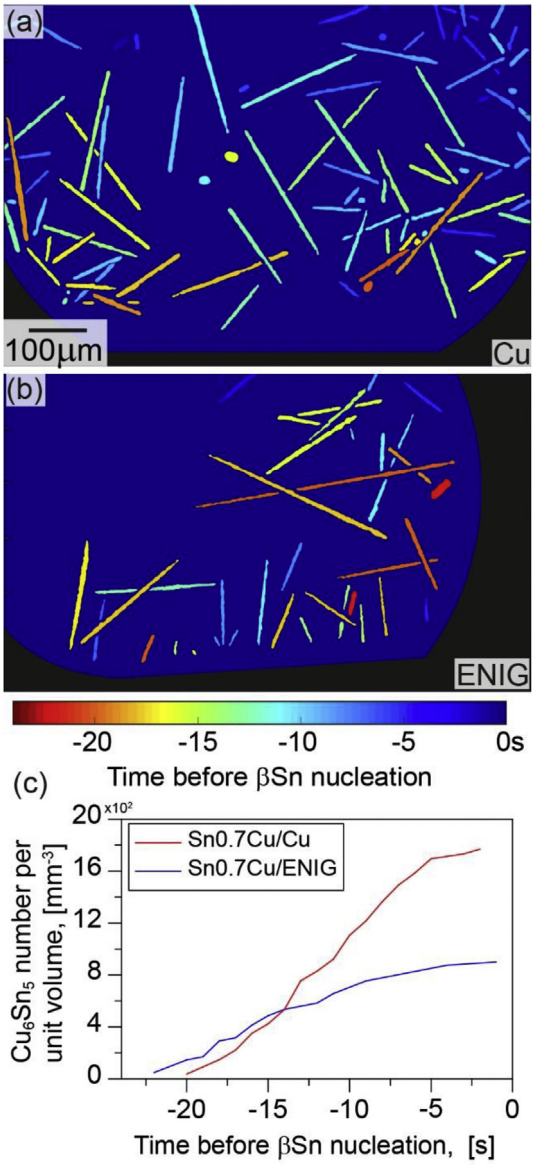

Fig. 5. (a)–(b): Processed maps corresponding to synchrotron image sequences of (a) Sn-0.7Cu/Cu, and (b) Sn-0.7Cu/ENIG from Fig. 4(a)–(b). Each Cu_6Sn_5 has been segmented and coloured by its nucleation time. t = −1s is the last frame prior to βSn nucleation. (c) Nucleation kinetics of primary Cu_6Sn_5 quantified from (a)–(b).

Table 2
Summary of the number density of Cu_6Sn_5 in Sn-0.7Cu/Cu, Sn-0.7Cu/ENIG, Sn-0.7Cu-0.05Ni/Cu, Sn-0.7Cu-0.05Ni/ENIG.

Type of solder joint	Cu_6Sn_5 number density, [mm^{-3}]
Sn-0.7Cu/Cu	1769
Sn-0.7Cu/ENIG	899
Sn-0.7Cu-0.05Ni/Cu	8595[a]
Sn-0.7Cu-0.05Ni/ENIG	7154

[a] Measurement is based on the top half in Fig. 4(c).

The primary Cu_6Sn_5 crystals are small and numerous and underwent significant motion due to gravity and convection. The motion was tracked using digital image correlation (DIC) and is shown in Fig. 4(e)-(f), where the arrows are displacement vectors of the crystals based on consecutive frames prior to βSn nucleation. It can be seen that the Cu_6Sn_5 particles are settling under gravity and are also being swept in a mostly clockwise convective flow.

The final number density of primary Cu_6Sn_5 in Sn-0.7Cu and Sn-0.7Cu-0.05Ni joints on Cu and ENIG from Fig. 4 are given in Table 2. It can be seen that the number density of Cu_6Sn_5 crystals in Sn-0.7Cu/ENIG is approximately half that of Sn-0.7Cu/Cu joints, which is related to the larger amount of Cu dissolved from the Cu substrate than Ni from ENIG. This also indicates that dissolved Ni from the ENIG is not effective at triggering primary Cu_6Sn_5 nucleation events. In contrast, in solders pre-alloyed with Ni, i.e. Sn-0.7Cu-0.05Ni, there are ~10 times more (Table 2) and smaller Cu_6Sn_5 crystals than in Sn-0.7Cu joints (compare Fig. 4a,b versus Fig. 4c,d). Note that for Sn-0.7Cu-0.05Ni/Cu in Fig. 4c, the number density measured in Table 2 is only based on the top half of the sample because the crystals in the bottom half are too small to quantify with the techniques used. Therefore, the true number density of primary Cu_6Sn_5 in Sn-0.7Cu-0.05Ni/Cu is even higher than in Table 2.

To test the generality of the synchrotron results in Fig. 4 and Table 2, solder foil and BGA joints were studied after reflow soldering in our laboratory. Fig. 6 compares the size and morphology of primary Cu_6Sn_5 crystals cooled from 250 °C in 1 cm^2 solder foil joints on Cu substrates. Fig. 6(a) and (b) are typical micrographs of Cu_6Sn_5 crystals, where it is clear that primary Cu_6Sn_5 are significantly smaller in Sn-0.7Cu-0.05Ni/Cu than in Sn-0.7Cu/Cu joints (note the different scale bars in Fig. 6(a) and (b)). The Cu_6Sn_5 size distributions from more than 100 crystals are quantified in Fig. 6(c) and the crystal width/length ratio is shown in Fig. 6(d). It can be seen that the mean crystal length is ~100 times smaller in Sn-0.7Cu-0.05Ni/Cu than in Sn-0.7Cu/Cu when the peak temperature was 250 °C.

Fig. 7(a) and (b) show a similar result for freestanding BGA balls of Sn-0.7Cu and Sn-0.7Cu-0.05Ni that were cooled from 250 °C: the primary Cu_6Sn_5 are at least an order of magnitude smaller in Sn-0.7Cu-0.05Ni than in Sn-0.7Cu (note the different scale bars in Fig. 7(a) and (b)). Table 2, Figs. 6 and 7(a) and (b) confirm that the strong grain refinement effect of Cu_6Sn_5 in Sn-0.7Cu-0.05Ni solder and joints is a general phenomenon when the peak temperature is 250 °C. In contrast, Ni has no significant grain refining effect on primary Cu_6Sn_5 when freestanding solders are heated to 400 °C (Fig. 1) nor when Ni is dissolved in from an ENIG substrate (Fig. 4(b) and Table 2).

Therefore, it seems that the mechanism of primary Cu_6Sn_5 size refinement in Sn-0.7Cu-0.05Ni is related with the partial remelting of Cu_6Sn_5 at 250 °C (~40 K below the Cu_6Sn_5 liquidus of Sn-0.7Cu-0.05Ni). To test this interpretation, a further experiment was conducted in which Sn-0.7Cu-0.05Ni solder balls were made by heating balls to 300 °C (where all Cu_6Sn_5 melts) with flux and then cooling at either 0.03 K/s or ~20 K/s. These solder balls containing large or small Cu_6Sn_5 were then soldered to Cu substrates with a peak temperature of 250 °C and a cooling rate of ~3 K/s in all cases. Typical examples of the resulting joints are shown in Fig. 8(a)-(d). It can be seen that joints made with solder balls initially containing large Cu_6Sn_5, contain large Cu_6Sn_5 after reflow that spans the entire width of the solder joint (Fig. 8(c)); whereas joints made with solder balls initially containing small Cu_6Sn_5, contain numerous small primary Cu_6Sn_5 after reflow (Fig. 8(a) and (b)). This confirms that the mechanism of Cu_6Sn_5 grain refinement in Sn-0.7Cu-0.05Ni is that pre-existing Cu_6Sn_5 particles are not fully melted during reflow and demonstrates that the size of primary Cu_6Sn_5 in Sn-0.7Cu-0.05Ni can be controlled by controlling the size of Cu_6Sn_5 in the initial solder ball. We note that Cu_6Sn_5 are usually very small in industrial Sn-0.7Cu-0.05Ni/Cu joints because the cooling rate is high in the initial manufacture of solder balls for BGAs, or powder for solder paste.

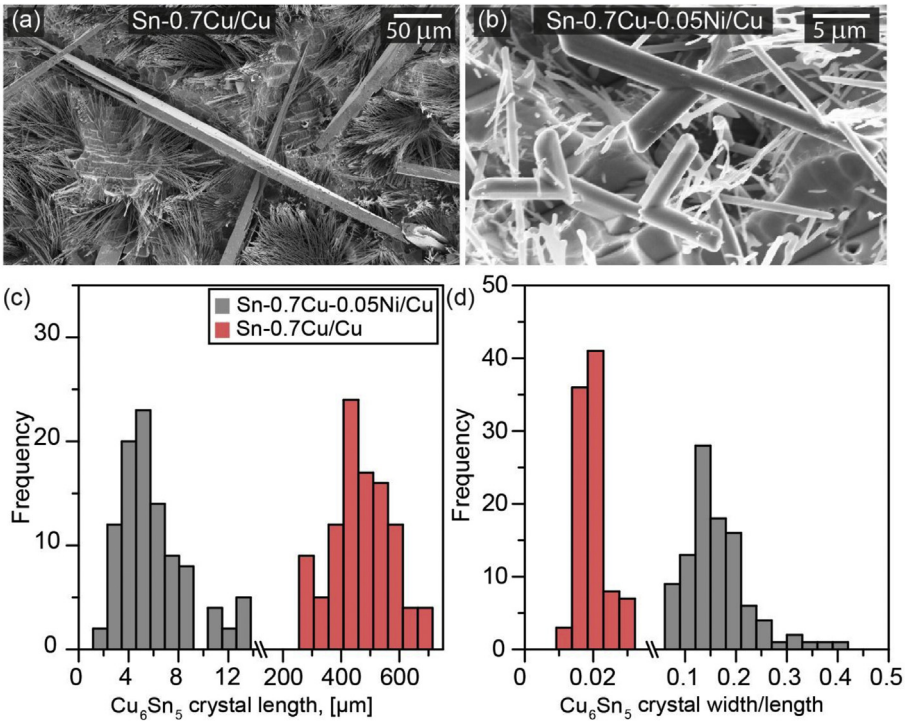

Fig. 6. Quantification of crystal sizes in Sn-0.7Cu/Cu and Sn-0.7Cu-0.05Ni/Cu. (a–b) Deep etched crystals in solder foils. Histogram of the crystal size in the solder foils are shown for (c) Cu_6Sn_5 crystal length and (d) Cu_6Sn_5 crystal width/length ratio.

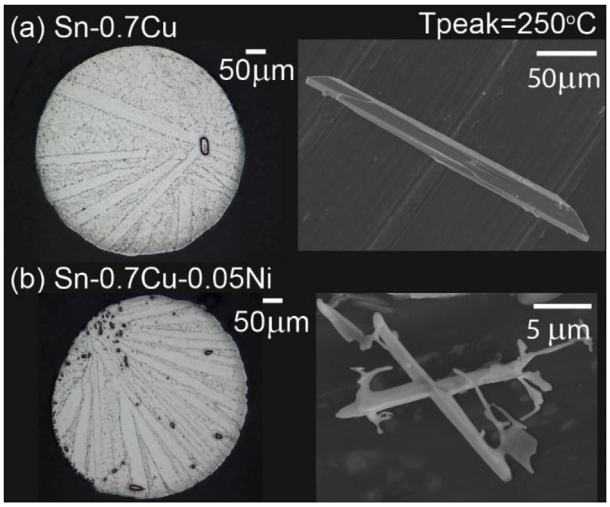

Fig. 7. Typical primary Cu_6Sn_5 crystals in freestanding solder balls after cooling at 0.33 K/s from 250 °C.

In contrast, in Ni-free Sn-0.7Cu/Cu joints, primary Cu_6Sn_5 all melts during reflow and the size of primary Cu_6Sn_5 depends only on the reflow profile.

3.3. *Twinning in $(Cu,Ni)_6Sn_5$ and Cu_6Sn_5*

A further phenomenon in Sn-0.7Cu-0.05Ni was that the Cu_6Sn_5 crystals were often X-shaped and multi-branched as can be seen in the micrographs in Fig. 4(c), (d), 6(b), 7(b), and 8(b). This can be further seen in Fig. 6(d) where the width/length ratio is increased by an order of magnitude in Sn-0.7Cu-0.05Ni, indicating that the shape of primary Cu_6Sn_5 with Ni is more equiaxed and more branched than Cu_6Sn_5 in Sn-0.7Cu/Cu joints.

The formation of branched Cu_6Sn_5 was studied by directly measuring the growth of X-shaped Cu_6Sn_5 crystals in Sn-0.7Cu-0.05Ni/ENIG joints in synchrotron image sequences. Fig. 9(a) shows aligned synchrotron radiographs of a moving crystal in Fig. 4(f) at different times after its nucleation. The moving crystal was aligned and centred using shift and rotation correction function in Davis. The coloured map in Fig. 9(b) has been generated similar to that in Fig. 1 but here each pixel is coloured individually by the time it becomes solid. From Fig. 9(b), it is clear that the X-shaped crystal nucleates from its centre and grows along four directions. Some Cu_6Sn_5 crystals had three branches like the ones shown in Fig. 6(b) and these are likely to have grown along three directions only.

The growth crystallography of X-shaped crystals was explored using extracted crystals such as the one shown in Fig. 10. Fig. 10(a) shows a complete X-shaped Cu_6Sn_5 crystal extracted from a ~∅500 µm Sn-0.7Cu-0.05Ni solder ball and its centre region is magnified in Fig. 10(b). Using EBSD, IPF-Y mapping was performed on the central area as shown in Fig. 10(c) where the background image is tilt corrected. The measured Cu_6Sn_5 orientations and corresponding unit cells are superimposed on the crystal in Fig. 10(b). It can be seen that the X-shaped Cu_6Sn_5 consists of two crystallographic orientations (pink and purple) and the growth crystallography in each arm of the X is the same as that reported previously for hexagonal Cu_6Sn_5 rods [20,29,30,43,48–51], i.e. growing in the [0001] direction with growth facets of $\{10\bar{1}0\}$. Fig. 10(d) shows corresponding pole figures of four important planes in

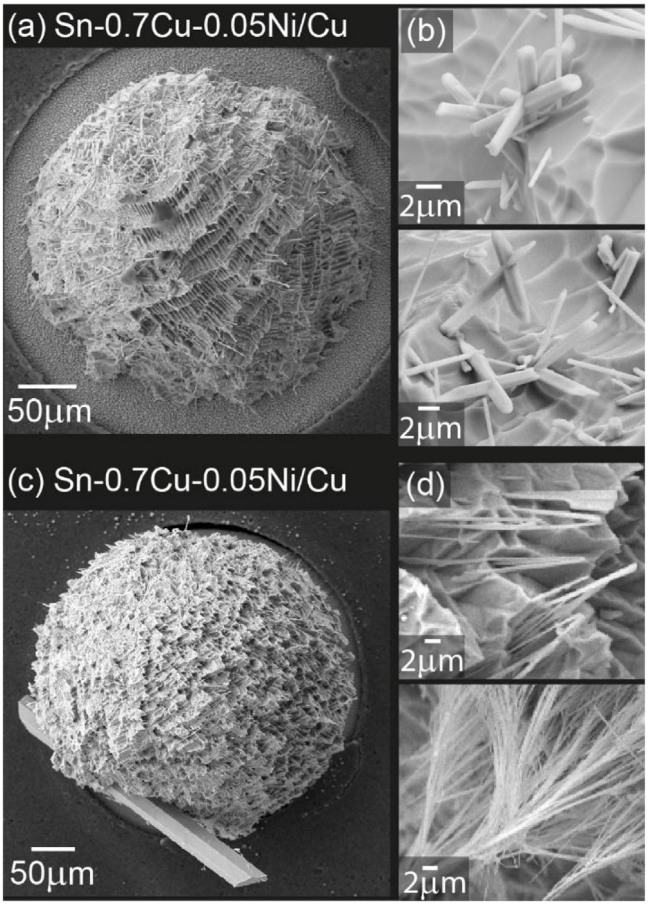

Fig. 8. Controlling the size of primary Cu_6Sn_5 in Sn-0.7Cu-0.05Ni/Cu joints. (a) A solder ball was initially fast cooled at ~20 K/s from 300 °C then soldered on Cu with a peak T of 250 °C and a cooling rate of ~3 K/s. (b) Fine X-shaped and multi-branched primary Cu_6Sn_5 crystals in (a). (c) A solder ball initially cooled at 0.03 K/s from 300 °C then soldered on Cu with a peak T of 250 °C and a cooling rate of ~3 K/s. A large Cu_6Sn_5 rod spans the entire joint. (d) Only eutectic Cu_6Sn_5 exist at higher magnification in (c).

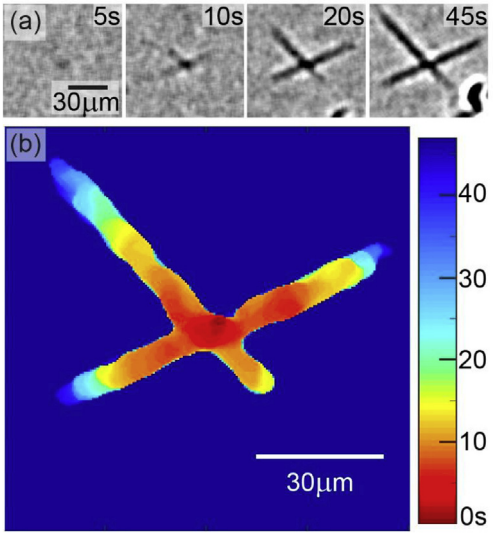

Fig. 9. (a) Aligned images of the X-shaped crystal in Fig. 4(f). (b) The coloured map has been processed with each pixel coloured by the time it becomes solid. Noise has been reduced using a median filter (5 × 5 pixels).

hexagonal Cu_6Sn_5. It can be seen that the two orientations share common $\{11\bar{2}0\}$, $\{10\bar{1}1\}$ and $\{10\bar{1}2\}$. From 49 pairs of twinned X-shaped Cu_6Sn_5 arms, the angle between the two [0001] directions was ~70.6 ± 0.5° and there were always common (shared) $\{11\bar{2}0\}$, $\{10\bar{1}1\}$ and $\{10\bar{1}2\}$ planes.

The ~70° angle combined with shared $\{11\bar{2}0\}$, $\{10\bar{1}1\}$ and $\{10\bar{1}2\}$ common planes is consistent with growth twinning as shown in Fig. 11 based on EBSD measurements. Fig. 11(a) shows an EBSD IPF-X map of the cross section of an X-shaped Cu_6Sn_5 crystal in Sn-0.7Cu-0.05Ni. Note that apparent X-shaped cross sections were preferentially studied because they have long arms lying in the cross section, which equivalently have < 0001 > pointing close to the circumference of the pole figure, making it easier to identify common and twin planes as shown in Fig. 11(b). Referring to Fig. 11(a–b), the EBSD mapping plane (i.e. centre of the pole figure) is near-parallel with the marked common plane in the $\{11\bar{2}0\}$ pole figure. The blue and red arrows are along the growth directions < 0001 > and are superimposed on [0001] poles near the top and right part of the circumference in Fig. 11(b). Two types of twin/interfacial planes are marked in Fig. 11(a) with projected plane normals shown by respective black arrows. Fig. 11(b) shows that the projected twin plane normals are through the common circled $\{10\bar{1}2\}$ and $\{10\bar{1}1\}$ poles, which are necessary conditions for twin planes being the $\{10\bar{1}2\}$ and $\{10\bar{1}1\}$ planes. 20 pairs of Cu_6Sn_5 crystals with clear boundaries similar to Fig. 11(a) were analysed. 20 out of 20 had $\{10\bar{1}1\}$ as the interfacial plane while 7 out of 20 had $\{10\bar{1}2\}$ coexisting as another interfacial plane. It is very likely that the $\{10\bar{1}1\}$ is the most common twin/interfacial plane, while the $\{10\bar{1}2\}$ twin plane can also coexist with $\{10\bar{1}1\}$. These two types of twin are common in hexagonal metals [52].

Fig. 11(c) is a low magnification atomic model of Cu_6Sn_5 growth twinning. The common $\{11\bar{2}0\}$planes are shown in projection where the two crystal lattices are orientated and coloured according to the IPF-X map in Fig. 11(a) and the macroscopic twin planes are shown. The atoms in Boxes A and B in Fig. 11(c) contain the $\{10\bar{1}2\}$ and $\{10\bar{1}1\}$ twin planes respectively, which are shown in more detail in Fig. 11(d) with two superimposed hexagonal unit cells. This is a type of penetration twinning with two distinct twin planes. If the red and blue rods are perfect single crystals, these twin planes cannot be crystallographically satisfied at the same time because the sum of the α_1 and α_2 angles in Figs. 11(d), 71.12°+110.06° = 181.18°(assuming binary Cu_6Sn_5 at 250 °C), is larger than 180°. Note in Fig. 11(d), that the standard twinning angle for the $\{10\bar{1}2\}$ type twin is 180-α_2, but we use α_2 to better indicate the angular mismatch between the two twin types. Since $\alpha_1 + \alpha_2 = 181.2°$ is 1.2° from 180°, it can be compensated by lattice defects/dislocations which enables both $\{10\bar{1}2\}$ and $\{10\bar{1}1\}$ twin planes to coexist in one penetration twinned bicrystal. Coexisting $\{10\bar{1}2\}$ and $\{10\bar{1}1\}$ twins are possible in Cu_6Sn_5 because this crystal is pseudo-cubic [53], with a c/a ratio of 1.21 which is close to the pseudo-cubic ratio of $\sqrt{3/2}$, ~1.22.

This type of twinning also led to multi-twinned Cu_6Sn_5 crystals. An example can be found in Fig. 8(b). Fig. 12 shows that multiple twinning can form following the same twin rules observed in Fig. 11. In Fig. 12(a), the left X-shaped crystal is the same penetration twin-type as Fig. 11 with only two orientations in the arms, while the right crystal has an additional third orientation near the centre of the crystal. The three different orientations are marked '1–3', where '1' and '2' have their [0001] almost in the plane of the screen and '3' has [0001] nearly pointing out of the screen. Fig. 12(b) shows the pole figures of the right multiple twinned crystal. The poles marked with 1 and 2 are the same as ones shown in Figs. 10 and 11; The [0001] of orientation '3' is also at 70° from both '1' and '2', and arm '3' shares common $\{11\bar{2}0\}$ planes with the other two arms respectively. Therefore, the '3'rd arm on the right crystal forms the same twinning with arms '1–2', and these three arms are multiple twinned, which is consistent with the morphology of the tri-crystal in Fig. 8(b). Multiple twinning were also found with more than three orientations in one crystal, and each twin segment within

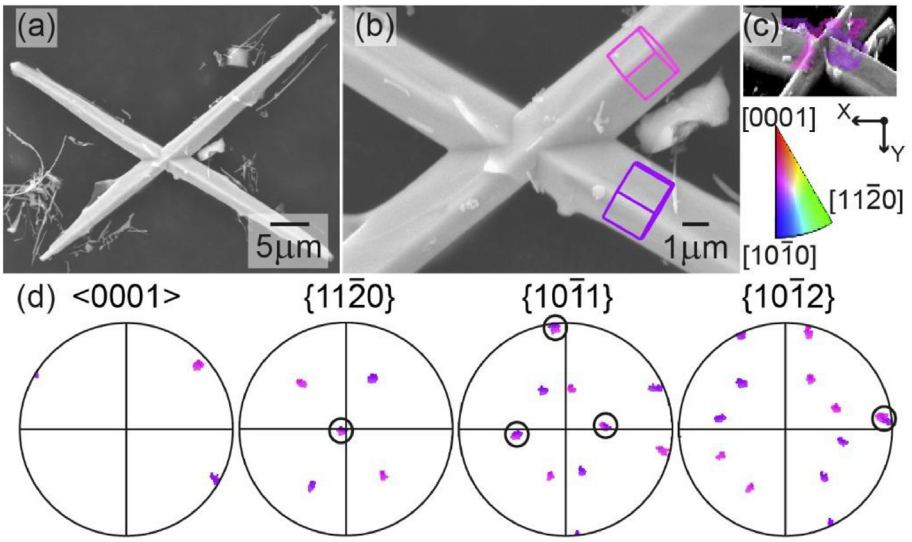

Fig. 10. (a) An extracted X-shaped Cu_6Sn_5 crystal in Sn-0.7Cu-0.05Ni solder balls. (b) The central part of the crystal with superimposed unit cells. (c) IPF-Y map of the centre superimposed on tilt corrected SE image. (d) Selected pole figures. Circles mark parallel planes.

each pair was consistent with Fig. 11.

It was found that X-shaped twinned crystals only formed when a peak temperature of ~250 °C was used. At peak temperatures of 400 °C, freestanding Sn-0.7Cu-0.05Ni solidified with Cu_6Sn_5 that were single crystal hexagonal rods, similar to Fig. 1. This shows that Ni solute is not solely responsible for the twinning and that X-shaped twins are promoted by unmelted Cu_6Sn_5 particles when the peak temperature is ~250 °C. To prove this concept, a binary Sn-1.1Cu alloy with a liquidus temperature of ~240 °C (Fig. 3(a)) was partially melted at 233 °C (~0.5 mass% solid in Fig. 3(c)) then cooled at ~1.8 K/s. The composition of Sn-1.1Cu is shown in Table 1. Twinned X-shaped Cu_6Sn_5 crystals were found in Sn-1.1Cu among a settled layer of intermetallics but the frequency of twinning was ~53% (10 out of 19), which is much lower than ~85% (49 out of 58) in Sn-0.7Cu-0.05Ni. Here, the frequency is defined as twinned Cu_6Sn_5 crystals from all analysed touching crystals that seem to have a X-shape cross section. One example is shown in Fig. 13 where the orientations of the two main arms were measured using EBSD. The twinning orientation relationship in binary Sn-1.1Cu is the same as that for Sn-0.7Cu-0.05Ni shown in Figs. 10 and 11, with twin interfacial planes of {10$\bar{1}$1} and possibly {10$\bar{1}$2}. In Fig. 13, the interfacial planes (shaded) are drawn near the centre of the X-shaped crystal and outlined in the unit cells. The occurrence of twinning in binary Sn-1.1Cu reflowed below the Cu_6Sn_5 liquidus temperature shows that Ni is not necessary for Cu_6Sn_5 growth twinning and confirms that unmelted primary Cu_6Sn_5 particles promote the formation of twinned crystals.

The fact that twinning is more likely to occur when Ni is present might be due to the influence of Ni on the lattice parameters of Cu_6Sn_5. Fig. 11(e–f) shows the influence of Ni and temperature on the c/a ratio and $\alpha_1+\alpha_2$ angle (in Fig. 11(d)) using data from Refs. [45,54]. A temperature change from 30 °C to 250 °C only yields a marginal ~0.1° difference in the angular mismatch for fixed Ni contents. As more Ni is dissolved, the c/a ratio of Cu_6Sn_5 becomes closer to $\sqrt{3/2}$ and $\alpha_1+\alpha_2$ becomes closer to 180° of pseudo-cubic, improving the angular mismatch between the two twins (zero mismatch occurs at ~15 at% Ni at 250 °C). For binary Cu_6Sn_5 (Ni = 0 at%), a ~1.2° mismatch from 180° is sufficiently small for both twin types to coexist, and decreasing this mismatch may promote the increased formation of X-shaped crystals containing two co-existing twin planes.

To further explore the relationship between the Ni content and twinning, EDS measurements were taken along the length of Cu_6Sn_5 arms as shown in Fig. 14(a–b). The Ni EDS map of a multi-twinned Cu_6Sn_5 crystal is shown in Fig. 14(b) where the central area has a higher Ni content than the tips. Fig. 14(c) summarises the Ni content change based on EDS point analysis along the growth directions with a measurement spacing of 1.5 μm and the numbered curves correspond to marked arrows in Fig. 14(a–b). It can be seen that the Ni content generally decreases from ~13 at% Ni near the centre of the 'X' to ~3 at % Ni along the growing arms, but in a few cases the Ni content does not change much, and the mean Ni content remains low at 1–4 at%. Fig. 14(d) shows a weighted interval rank sort (WIRS) plot (developed in Ref. [55] for the study of microsegregation) of the data in Fig. 14(c) to give an indication of the composition profile along a one-dimensional Cu_6Sn_5 branch. The plot includes more than 240 EDX measurements along Cu_6Sn_5 branches with a 1.5 μm step size. It can be seen that the Sn content in Cu_6Sn_5 is near-constant, and that the Ni content decreases from ~13 at% Ni at the start of solidification down to ~0 at% Ni. Comparing Fig. 14(d) with Fig. 11 (e–f), it can be seen that the Ni content at the centre of X-crystals is ~13 at% Ni which is close to the Ni content (~15 at%) that gives perfectly pseudo-cubic Cu_6Sn_5 at 250 °C (the peak reflow temperature) where both {10$\bar{1}$2} and {10$\bar{1}$1} twin planes can coexist without strain or lattice defects.

We note that the common plane in the X-shaped crystals, {11$\bar{2}$0}, is the same as the Cu_6Sn_5-Cu interface plane of the 'rooftop-type' Cu_6Sn_5

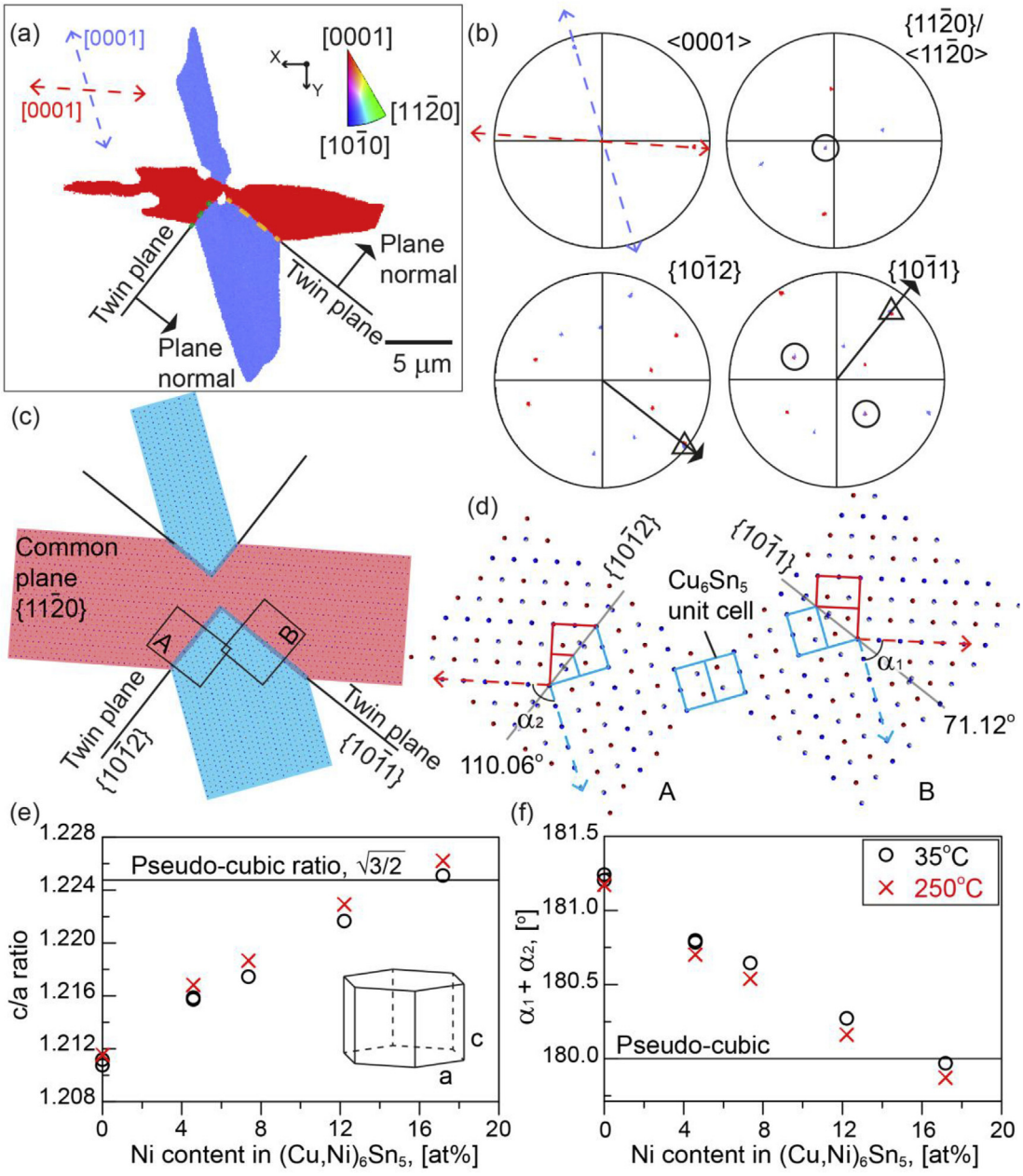

Fig. 11. (a) EBSD IPF-X map of a sectioned X-shaped Cu_6Sn_5 crystal. (b) Pole figures of selected planes and directions. Circles mark parallel planes, triangles mark twin interfaces. (c) Atomic model in the common plane. (d) Detailed atomic arrangement and twinning angles of the two twin interfaces {10$\bar{1}$2} and {10$\bar{1}$1}. (e–f) The influence of Ni on the c/a ratio and $\alpha1+\alpha2$ at two temperatures using data from Refs. [45,54].

morphology when Sn is soldered to {100} and/or {111} single crystal Cu substrates [18–22], and both the X-shaped crystals and 'rooftop-type' Cu_6Sn_5 have bounding facets of {10$\bar{1}$0}. However, in the case of a 'rooftop-type' Cu_6Sn_5 layer, the angle between the Cu_6Sn_5 is 90° or 60° due to the variants of the orientation relationships with Cu whereas, here, the angle between Cu_6Sn_5 is ~70° due to a twin orientation relationship. Note that the branching angle can also be ~40° for in-plane multiple-twinned crystals, e.g. the acute angle between crystal 3 and 5 in Fig. 14(b).

4. Conclusions

The influence of Ni on the solidification of primary Cu_6Sn_5 in Sn-0.7Cu-xNi has been studied in freestanding solders and solder joints on Cu and electroless-nickel-immersion-gold (ENIG) substrates using synchrotron radiography, EBSD and EDS analyses. The refinement and twinning of Cu_6Sn_5 due to a 500 ppm Ni addition have been measured and relevant mechanisms explored. The following conclusions can be drawn.

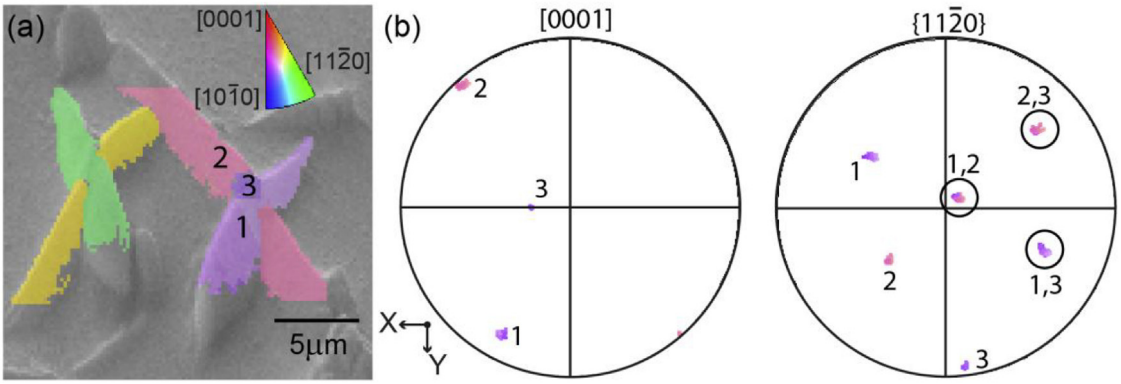

Fig. 12. (a) EBSD IPF-X map of sectioned X-shaped Cu_6Sn_5 crystals, the left is a simple X-shaped penetration twin while the right is a multiple twin. (b) Pole figures of the multiple twinning on the right X-shaped cross section.

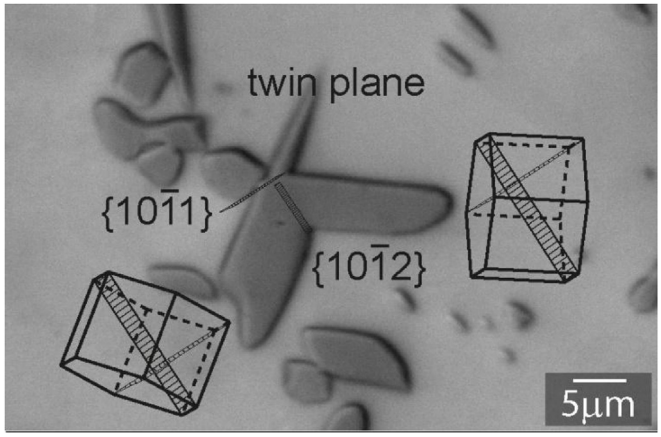

Fig. 13. Cross section of an X-shaped twinned Cu_6Sn_5 in a binary Sn-1.1Cu alloy, which was partially remelted at 233 °C. Wireframe unit cells were measured by EBSD.

- The 500 ppm Ni addition has been shown to only marginally increase the number density of primary Cu_6Sn_5 when the alloy is fully melted at 400 °C prior to solidification. Similarly, Ni dissolution from substrates in Sn-0.7Cu/ENIG joints does not refine the primary Cu_6Sn_5 size compared with Sn-0.7Cu/Cu joints. These results prove that Ni solute itself is not the dominant factor in Cu_6Sn_5 refinement in Sn-Cu-Ni solders.
- Ni additions strongly steepen the Cu_6Sn_5 liquidus slope and, in Sn-0.7Cu-0.05Ni, the Cu_6Sn_5 liquidus temperature is ~293 °C. Therefore, primary Cu_6Sn_5 does not fully remelt at typical reflow temperatures of ≤250 °C. As a result, the size of primary Cu_6Sn_5 in Sn-0.7Cu-0.05Ni after solidification strongly depends on the size of preceding primary Cu_6Sn_5 in the original solder ball/paste before melting. In the case of BGA sphere manufacturing, the high cooling rate creates numerous small primary Cu_6Sn_5 that are retained during reflow at 250 °C and act as numerous seeds for primary Cu_6Sn_5 growth during cooling. This is the main origin of primary Cu_6Sn_5 refinement in Ni-containing solders.
- X-shaped Cu_6Sn_5 crystals were common in Sn-0.7Cu-0.05Ni. They are observed to grow from the centre of the 'X' using synchrotron imaging. EBSD analysis showed that X-shaped Cu_6Sn_5 are a penetration twin with two distinct interfaces, {10$\bar{1}$2} or {10$\bar{1}$1}, which generates a fixed branching angle of ~70° around the <11$\bar{2}$0> twin axis.
- Twinned X-shaped Cu_6Sn_5 crystals were commonly found in Sn-0.7Cu-0.05Ni and were even observed in binary Sn-1.1Cu, provided the peak reflow temperature was below the Cu_6Sn_5 liquidus temperature.
- Cu_6Sn_5 solidification twinning was promoted by Ni additions. The maximum Ni content in Cu_6Sn_5 was shown to be at the centre of the 'X' where twinning originates. Reanalysis of past data on the influence of Ni on the Cu_6Sn_5 lattice parameters shows that the Ni content near the centre of twinned 'X'-crystals gives a c/a ratio that is close to perfectly pseudo-cubic which is expected to facilitate the formation of coexisting {10$\bar{1}$2} and {10$\bar{1}$1} twin planes, that are a key feature of X-shaped penetration twinning.

Acknowledgements

The authors gratefully acknowledge funding from Nihon Superior Co., Ltd.; the UK EPSRC (grant numbers EP/M002241/1 and EP/N007638/1: the Future LiME Hub); a President's scholarship from Imperial College London; and a Grant-in-Aid for Scientific Research (S) (24226018) from JSPS, Japan. Synchrotron experiments were conducted during SPring-8 beamtimes 2017B1519, 2016B1319, 2014B1620 and 2015A1675.

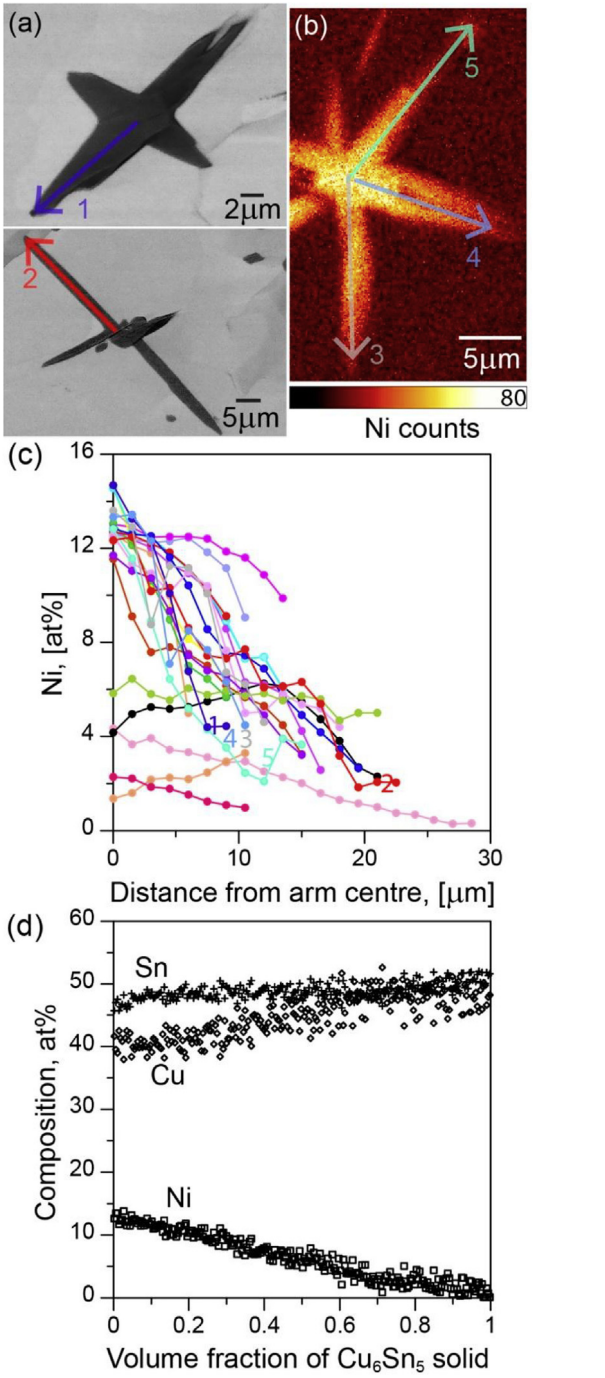

Fig. 14. (a) BSE images of X-shaped cross sections. (b) EDS mapping of Ni in a multi-twinned Cu_6Sn_5 crystal. (c) Ni content vs. distance along the arms of X-shaped crystals in Sn-0.7Cu-0.05Ni cooled from 250 °C, where the numbered curves correspond to marked arrows in (a–b). (d) Weighted interval ranked sort (WIRS) plot showing the compositional profile along a Cu_6Sn_5 branch.

References

[1] M. Laentzsch, Theory and practical experience of micro-alloyed SnCu0. 7NiGe (SN100C), Electron. Syst. Technol. 2006, pp. 383–386.

[2] W.H. Zhu, L. Xu, J.H.L. Pang, X.R. Zhang, E. Poh, Y.F. Sun, A.Y.S. Sun, C.K. Wang, H.B. Tan, Drop reliability study of PBGA assemblies with SAC305, SAC105 and SAC105-Ni solder ball on Cu-OSP and ENIG surface finish, Electron. Compon. Technol. Conf. 2008, pp. 1667–1672.

[3] H. Steen, B. Toleno, Development of a lead-free alloy for high-reliability, high-temperature applications, Proc. IPC APEX EXPO, 2010.

[4] R. Coyle, R. Parker, K. Howell, D. Hillman, J. Smetana, G. Thomas, S. Longgood, M. Osterman, E. Lundeen, P. Snugovsky, A collaborative industrial consortia program for characterizing thermal fatigue reliability of third generation Pb-free alloys, SMTA. Int. 2016, pp. 25–29.

[5] J.Y. Tsai, Y.C. Hu, C.M. Tsai, C.R. Kao, A study on the reaction between Cu and Sn3.5Ag solder doped with small amounts of Ni, J. Electron. Mater. 32 (2003) 1203–1208.

[6] T. Laurila, V. Vuorinen, M. Paulasto-Kröckel, Impurity and alloying effects on interfacial reaction layers in Pb-free soldering, Mater. Sci. Eng. R Rep. 68 (2010) 1–38.

[7] Y.W. Wang, Y.W. Lin, C.T. Tu, C.R. Kao, Effects of minor Fe, Co, and Ni additions on the reaction between SnAgCu solder and Cu, J. Alloy. Comp. 478 (2009) 121–127.

[8] C. Yang, F. Song, S.W. Ricky Lee, Impact of Ni concentration on the intermetallic compound formation and brittle fracture strength of Sn-Cu-Ni (SCN) lead-free solder joints, Microelectron. Reliab. 54 (2014) 435–446.

[9] G. Zeng, S.D. Mcdonald, D. Mu, Y. Terada, H. Yasuda, Q. Gu, K. Nogita, Intermetallics Ni segregation in the interfacial $(Cu,Ni)_6Sn_5$ intermetallic layer of Sn-0.7Cu-0.05Ni/Cu ball grid array (BGA) joints, Intermetallics 54 (2014) 20–27.

[10] S.A. Belyakov, J.W. Xian, K. Sweatman, T. Nishimura, T. Akaiwa, C.M. Gourlay, Influence of bismuth on the solidification of Sn-0.7Cu-0.05Ni-xBi/Cu joints, J. Alloy. Comp. 701 (2017) 321–334.

[11] C.-H. Lin, S.-W. Chen, C.-H. Wang, Phase equilibria and solidification properties of Sn-Cu-Ni alloys, J. Electron. Mater. 31 (2002) 907–915.

[12] C.Y. Li, G.J. Chiou, J.G. Duh, Phase distribution and phase analysis in Cu_6Sn_5, Ni_3Sn_4, and the Sn-rich corner in the ternary Sn-Cu-Ni isotherm at 240°C, J. Electron. Mater. 35 (2006) 343–352.

[13] C. Schmetterer, H. Flandorfer, C. Luef, A. Kodentsov, H. Ipser, Cu-Ni-Sn: a key system for lead-free soldering, J. Electron. Mater. 38 (2009) 10–24.

[14] C.M. Gourlay, K. Nogita, J. Read, A.K. Dahle, Intermetallic formation and fluidity in Sn-rich Sn-Cu-Ni alloys, J. Electron. Mater. 39 (2010) 56–69.

[15] K. Nogita, Stabilisation of Cu_6Sn_5 by Ni in Sn-0.7Cu-0.05Ni lead-free solder alloys, Intermetallics 18 (2010) 145–149.

[16] M. Tanaka, T. Sasaki, T. Kobayashi, K. Tatsumi, Improvement in drop shock reliability of Sn-1.2Ag-0.5Cu BGA interconnects by Ni addition, Electron. Compon. Technol. Conf. 2006, pp. 78–84.

[17] H. Tsukamoto, T. Nishimura, S. Suenaga, S.D. McDonald, K.W. Sweatman, K. Nogita, The influence of solder composition on the impact strength of lead-free solder ball grid array joints, Microelectron. Reliab. 51 (2011) 657–667.

[18] J.O. Suh, K.N. Tu, N. Tamura, A synchrotron radiation x-ray microdiffraction study on orientation relationships between a Cu_6Sn_5 and Cu substrate in solder joints, JOM 58 (2006) 63–66.

[19] J.O. Suh, K.N. Tu, N. Tamura, Dramatic morphological change of scallop-type Cu_6Sn_5 formed on (001) single crystal copper in reaction between molten SnPb solder and Cu, Appl. Phys. Lett. 91 (2007) 051907.

[20] Y. Tian, R. Zhang, C. Hang, L. Niu, C. Wang, Relationship between morphologies and orientations of Cu_6Sn_5 grains in Sn3.0Ag0.5Cu solder joints on different Cu pads, Mater. Char. 88 (2014) 58–68.

[21] H.F. Zou, H.J. Yang, Z.F. Zhang, Morphologies, orientation relationships and evolution of Cu_6Sn_5 grains formed between molten Sn and Cu single crystals, Acta. Mater 56 (2008) 2649–2662.

[22] Z. Zhang, H. Cao, M. Li, Y. Yu, H. Yang, S. Yang, Three-dimensional placement rules of Cu_6Sn_5 textures formed on the (111)Cu and (001)Cu surfaces using electron backscattered diffraction, Mater. Des. 94 (2016) 280–285.

[23] D. Mu, H. Yasuda, H. Huang, K. Nogita, Growth orientations and mechanical properties of Cu_6Sn_5 and $(Cu,Ni)_6Sn_5$ on poly-crystalline Cu, J. Alloy. Comp. 536 (2012) 38–46.

[24] S. Chada, R.A. Fournelle, W. Laub, D. Shangguan, Copper substrate dissolution in eutectic Sn-Ag solder and its effect on microstructure, Energy 29 (2000) 1214–1221.

[25] D. Frear, D. Grivas, J.W. Morris, The effect of Cu_6Sn_5 whisker precipitates in bulk 60Sn-40Pb solder, J. Electron. Mater. 16 (1987) 181–186.

[26] M.O. Alam, Y.C. Chan, K.N. Tu, Effect of 0.5 wt% Cu addition in Sn-3.5%Ag solder on the dissolution rate of Cu metallization, J. Appl. Phys. 94 (2003) 7904–7909.

[27] J. Keller, D. Baither, U. Wilke, G. Schmitz, Mechanical properties of Pb-free SnAg solder joints, Acta Mater. 59 (2011) 2731–2741.

[28] M.A.A. Mohd Salleh, C.M. Gourlay, J.W. Xian, S.A. Belyakov, H. Yasuda, S.D. McDonald, K. Nogita, In situ imaging of microstructure formation in electronic interconnections, Sci. Rep. 7 (2017).

[29] Z.H. Zhang, H.J. Cao, H.F. Yang, M.Y. Li, Y.X. Yu, Hexagonal-rod growth mechanism and kinetics of the primary Cu_6Sn_5 phase in liquid Sn-based solder, J. Electron. Mater. 45 (2016) 5985–5995.

[30] J.W. Xian, S.A. Belyakov, C.M. Gourlay, Controlling bulk Cu_6Sn_5 nucleation in Sn0.7Cu/Cu joints with Al micro-alloying, J. Electron. Mater. 45 (2016) 69–78.

[31] Z.Q. Li, S.A. Belyakov, J.W. Xian, C.M. Gourlay, The influence of primary Cu_6Sn_5 size on the shear impact properties of Sn-Cu/Cu BGA joints, J. Electron. Mater. 47 (2018) 84–95.

[32] M.A.A. Mohd Salleh, S.D. McDonald, C.M. Gourlay, S.A. Belyakov, H. Yasuda, K. Nogita, Effect of Ni on the formation and growth of primary Cu_6Sn_5 intermetallics in Sn-0.7wt.%Cu solder pastes on Cu substrates during the soldering process, J. Electron. Mater. 45 (2015) 154–163.

[33] C.M. Gourlay, S.A. Belyakov, Z.L. Ma, J.W. Xian, Nucleation and growth of tin in Pb-free solder joints, JOM 67 (2015) 2383–2393.

[34] G. Zeng, S. Xue, L. Zhang, L. Gao, Z. Lai, J. Luo, Properties and microstructure of Sn-0.7Cu-0.05Ni solder bearing rare earth element Pr, J. Mater. Sci. Mater. Electron. 22 (2011) 1101–1108.

[35] J.W. Yoon, Y.H. Lee, D.G. Kim, H.B. Kang, S.J. Suh, C.W. Yang, C.B. Lee, J.M. Jung, C.S. Yoo, S.B. Jung, Intermetallic compound layer growth at the interface between Sn-Cu-Ni solder and Cu substrate, J. Alloy. Comp. 381 (2004) 151–157.

[36] A.E. Hammad, Investigation of microstructure and mechanical properties of novel Sn–0.5Ag–0.7Cu solders containing small amount of Ni, Mater. Des. 50 (2013) 108–116.
[37] F. Cheng, H. Nishikawa, T. Takemoto, Microstructural and mechanical properties of Sn-Ag-Cu lead-free solders with minor addition of Ni and/or Co, J. Mater. Sci. 43 (2008) 3643–3648.
[38] G. Zeng, S.D. McDonald, Q. Gu, Y. Terada, K. Uesugi, H. Yasuda, K. Nogita, The influence of Ni and Zn additions on microstructure and phase transformations in Sn-0.7Cu/Cu solder joints, Acta Mater. 83 (2015) 357–371.
[39] B. Lee, H. Jeon, K. Kwon, H. Lee, Employment of a bi-layer of Ni(P)/Cu as a diffusion barrier in a Cu/Sn/Cu bonding structure for three-dimensional interconnects, Acta Mater. 61 (2013) 6736–6742.
[40] S.W. Chen, C.H. Wang, Interfacial reactions of Sn-Cu/Ni couples at 250°C, J. Mater. Res. 21 (2006) 2270–2277.
[41] C. Wang, S. Chen, Sn–0.7wt.%Cu/Ni interfacial reactions at 250°C, Acta Mater. 54 (2006) 247–253.
[42] O. Saliza Azlina, A. Ourdjini, Influence of difference solders volume on intermetallic growth of Sn-4.0Ag-0.5Cu/ENEPIG, MATEC Web of Conferences, 2016 01073.
[43] J.W. Xian, S.A. Belyakov, M. Ollivier, K. Nogita, H. Yasuda, C.M. Gourlay, Cu_6Sn_5 crystal growth mechanisms during solidification of electronic interconnections, Acta Mater. 126 (2017) 540–551.
[44] B. Peplinski, G. Schulz, D. Schultze, E. Schierhorn, Improved X-ray powder diffraction data for the disordered η-Cu_6Sn_5 alloy phase, Mater. Sci. Forum 228–231 (1996) 577–582.
[45] K. Nogita, C.M. Gourlay, T. Nishimura, Cracking and phase stability in reaction layers between Sn-Cu-Ni solders and Cu substrates, JOM 61 (2009) 45–51.
[46] Thermo-Calc, TCSLD Database Version 3.0, (2015).
[47] V. Vuorinen, H. Yu, T. Laurila, J.K. Kivilahti, Formation of intermetallic compounds between liquid Sn and various $CuNi_x$ metallizations, J. Electron. Mater. 37 (2008) 792–805.
[48] Y. Tian, L. Niu, C. Wang, Analysis of Cu_6Sn_5 grain orientations in Sn3.0Ag0.5Cu lead-free solder joints, ICEPT-HDP (2011) 353–356.
[49] J.W. Xian, S.A. Belyakov, T.B. Britton, C.M. Gourlay, Heterogeneous nucleation of Cu_6Sn_5 in Sn-Cu-Al solders, J. Alloy. Comp. 619 (2015) 345–355.
[50] M. Yang, Y. Cao, S. Joo, H. Chen, X. Ma, M. Li, Cu_6Sn_5 precipitation during Sn-based solder/Cu joint solidification and its effects on the growth of interfacial intermetallic compounds, J. Alloy. Comp. 582 (2014) 688–695.
[51] Y. Zhong, N. Zhao, C.Y. Liu, W. Dong, Y.Y. Qiao, Y.P. Wang, H.T. Ma, Continuous epitaxial growth of extremely strong Cu_6Sn_5 textures at liquid-Sn/(111)Cu interface under temperature gradient, Appl. Phys. Lett. 111 (2017) 223502.
[52] E. Tenckhoff, Review of deformation mechanisms, texture, and mechanical anisotropy in zirconium and zirconium base alloys, J. ASTM Int. 2 (2005) 25–50.
[53] S. Lidin, Superstructure ordering of intermetallics: B8 structures in the pseudo-cubic regime, Acta Crystallogr. Sect. B Struct. Sci. 54 (1998) 97–108.
[54] K. Nogita, D. Mu, S.D. McDonald, J. Read, Y.Q. Wu, Effect of Ni on phase stability and thermal expansion of $Cu_{6-x}Ni_xSn_5$(x = 0, 0.5, 1, 1.5 and 2), Intermetallics 26 (2012) 78–85.
[55] M. Ganesan, D. Dye, P.D. Lee, A technique for characterizing microsegregation in multicomponent alloys and its application to single-crystal superalloy castings, Metall. Mater. Trans. 36 (2005) 2191–2204.